Applied Thermal Engineering 193 (2021) 116945

Contents lists available at ScienceDirect

Applied Thermal Engineering

journal homepage: www.elsevier.com/locate/apthermeng

Melting process of the nano-enhanced phase change material (NePCM) in an optimized design of shell and tube thermal energy storage (TES): Taguchi optimization approach

Mohammad Ghalambaz [a,b], S.A.M. Mehryan [c], Ali Veismoradi [d], Mahboobeh Mahdavi [e], Iman Zahmatkesh [f], Zahra Kazemi [g], Obai Younis [h,i], Mehdi Ghalambaz [j,k,*], Ali J. Chamkha [l]

[a] Metamaterials for Mechanical, Biomechanical and Multiphysical Applications Research Group, Ton Duc Thang University, Ho Chi Minh City, Vietnam
[b] Faculty of Applied Sciences, Ton Duc Thang University, Ho Chi Minh City, Vietnam
[c] Young Researchers and Elite Club, Yasooj Branch, Islamic Azad University, Yasooj, Iran
[d] Chemical Engineering Department, Ferdowsi University, Mashhad, Iran
[e] Mechanical Engineering Department, Gannon University, 109 University Square, Erie, PA 16541, USA
[f] Department of Mechanical Engineering, Mashhad Branch, Islamic Azad University, Mashhad, Iran
[g] Department of Mechanical Engineering, Shiraz University, Shiraz 71936, Iran
[h] Department of Mechanical Engineering, College of Engineering at Wadi Addwaser, Prince Sattam Bin Abdulaziz University, Saudi Arabia
[i] Department of Mechanical Engineering, Faculty of Engineering, University of Khartoum, Sudan
[j] Institute of Research and Development, Duy Tan University, Da Nang 550000, Vietnam
[k] Faculty of Electrical – Electronic Engineering, Duy Tan University, Da Nang 550000, Vietnam
[l] Faculty of Engineering, Kuwait College of Science and Technology, Doha Area, Kuwait

ARTICLE INFO

Keywords:
Thermal Energy Storage (TES) unit
Petal-pipe
Design optimization
Shell and tube heat exchanger

ABSTRACT

The thermal performance and response time of Thermal Energy Storage (TES) units are mainly limited by the enclosure design and the low thermal conductivity of the storage medium. In the present study, the performance of petal-shape pipes in a shell and tube TES unit was numerically modeled and analyzed. The integration of the finite element method, a mesh adaptation approach, and an adaptive time-step scheme, was used to robustly simulate the phase change process and energy storage in the TES unit. The enclosure was considered fixed both dimensionally and by volume, which acts as a design constraint. The impacts of using two types of nano-additives, Cu and GO nanoparticles, and the geometrical aspects of the petal pipe on the thermal behavior of the TES unit were investigated. To find the optimal design of the TES unit with the maximum thermal energy power, the Taguchi optimization method was employed and a sensitivity analysis was performed. The copper nano-additives showed a better performance than the graphene oxide nano-additives. Although the surface area of the petal-pipe was fixed, its geometric shape was the most important parameter for maximizing the energy storage power of the TES unit. The optimum design could improve the amount of storage energy by 23.3% (Cu) and 22.5% (GO) NePCM compared to average designs. Based on an ANOVA analysis, the amplitude of petal shape could influence the total energy storage with a contribution ratio of about 41%, while the nanoparticles' contribution was 5–6%. An optimal design of a petal tube and Cu nanoparticles could improve the heat transfer by 45% compared to a circular tube with no nanoparticles.

1. Introduction

Modern engineering applications demand the use of Thermal Energy Storage (TES) systems that can effectively store thermal energy. Among the various TES options, a commonly employed method is the use of Latent Heat Thermal Energy Storage (LHTES), where the latent heat of a Phase Change Material (PCM) during the solid-liquid phase change is used to absorb or release energy. LHTES systems are preferred as they offer heat transfer at a nearly constant operating temperature, and they have larger energy densities. Recently, LHTES systems have been incorporated into solar power generation, electronic devices, and domestic HVAC systems. Comprehensive reviews of this field have been

* Corresponding author.
E-mail addresses: mohammad.ghalambaz@tdtu.edu.vn (M. Ghalambaz), mehdighalambaz@duytan.edu.vn (M. Ghalambaz).

https://doi.org/10.1016/j.applthermaleng.2021.116945
Received 22 November 2020; Received in revised form 17 March 2021; Accepted 5 April 2021
Available online 15 April 2021
1359-4311/

recently reported by Faraj et al. Li et al. [1] Javadi et al. [2] Wu et al. [3] and Katekar et al. [4].

In spite of the ability of the PCMs to store and release large amounts of energy, they inherently have a low thermal conductivity that is usually in the range of 0.2–0.7 W/m·K [5]. The low thermal conductivity of the PCM slows down the heat transfer process during the storage and release of energy, thereby elevating the response time of the PCMs. This drawback impedes the efficiency of TES systems utilizing PCMs. To overcome this shortcoming, nano-additives (such as nanoparticles, nanofibers, nanotubes, or nanosheets) with high thermal conductivities can be dispersed into the PCMs. The resulting suspension is referred to as Nano-enhanced Phase Change Materials (NePCMs), which provide a new type of working fluid for efficient TES systems. Xiong et al. [5] Tariq et al. [6] Nižetić et al. [7] Jebasingh and Arasu [8] and Yang et al. [9] have conducted insightful research on the thermophysical properties, preparation techniques, and applications of the NePCMs. Some of the studies regarding the thermal fluid characteristics of NePCM during and melting and solidification processes are presented here.

The charging process and heat transfer utilizing NePCM inside a two-layered channel were reported by Sheikholeslami et al. [10]. The upper layer contained the NePCM, while hot air flowed through the lower layer. It was observed that the maximum heat storage occurred at lower times as the nano-additive volume fraction increased.

The improvement in the performance of LHTES systems can be achieved by increasing the heat transfer surface area. The insertion of fins and variations in the geometrical configuration of the enclosure are two available methods to this aim. These methods have been successful for heat transfer enhancement in conventional enclosures, and lots of works are available in the literature to address this issue. In the literature, some studies adopted one of these two strategies for the performance improvement of TES systems utilizing the PCMs or NePCMs: Yehya and Naji [11] determined the optimum configuration of a rectangular enclosure for heat transfer enhancement of the PCMs. Bayat et al. [12] simulated a finned heat sink working with the NePCMs. Bondareva et al. [13] discussed the heat transfer performance of a finned tilted enclosure occupied by the NePCMs. The solidification of a hybrid NePCM in an annulus was investigated by Hosseinzadeh et al. [14]. A tree-like branching fin was implemented to increase the heat transfer rate from the heat source to the PCM.

The heat transfer surface of the smooth tube containing the heat transfer fluid (HTF) is limited, which influences its efficiency in the rate of energy storage. For this purpose, the smooth tube in LHTES unit can be redesigned to better its thermal performance. The heat transfer surface of the tube can be modified by using corrugated and quesi-petal, zigzag, and grooved configurations [15–18]. Ren [15] improved the energy storage rate in a NePCM-filled square container by employing the quesi-petal surfaces. Mahani et al. [18] studied the melting process in a zigzag plate Latent Heat Storage unit. They observed that much better improvement is reached by the zigzag structure in comparison to the smooth structure.

The effects of both strategies (i.e., the fin insertion and shape of the NePCM container) were compared with the influence of the nano-additive dispersion in the study of Singh et al. [19]. To this aim, they simulated a finned, conical-shaped TES system. The conical-shaped container was accompanied by a 16% reduction in the melting time. Additionally, the fin insertion provided a higher heat transfer elevation as compared to the nano-additive dispersion.

In this work, simulation and optimization of the melting and solidification processes of the NePCMs in a heat exchanger energy storage system are presented. The LHTES system is composed of a quasi-petal tube and a shell where the NePCM is located. To optimize the performance of the system, the Taguchi experimental design method is implemented. This method is a useful technique to find the optimum combination of different levels of various control factors as it requires a limited number of experimental or numerical trials. We also apply the analysis of variance (ANOVA) to the results of the Taguchi method. This evaluates the effectiveness of each control factor on the response of the heat exchanger energy storage system.

In the literature, several studies implemented the Taguchi method and ANOVA to optimize the performance of thermal systems. Some recent works are as follows: Alinejad and Esfahani [20] discussed the application of the Taguchi method in a three-dimensional turbulent mixed convection heat transfer. Sobhani et al. [21] analyzed the factors affecting the combined radiation-natural convection heat transfer in an enclosure with horizontal fins adopting this method. The Taguchi technique was adopted by Zahmatkesh and Shandiz [22] to determine the optimal combination of key parameters in magnetohydrodynamics heat transfer of nanofluids in porous cavities. Nath and Krishnan [23] utilized the Taguchi method for double-diffusive mixed convection of nanofluids in a backward-facing step. Tang et al. [24] applied the Taguchi method to the hydrodynamics and heat transfer of nanofluids flowing through a channel in the presence of longitudinal vortex generators. Sharifi et al. [25] determined proper surfactants for the stabilization of a nanofluid through the Taguchi method. Biçer et al. [26] utilized the Taguchi method to optimize a shell-and-tube heat exchanger with a novel baffle design. Moreover, the efficiency and the thermal power of a portable solar cooker were optimized using the Taguchi method by Hosseinzadeh et al. [27].

As discussed above, various aspects of phase change heat transfer and energy storage in TES units have been individually investigated in the literature. However, the combination of nano-additives and the optimized design of the TES unit is a novel approach. The presence of nanoparticles could influence the heat transfer and convection heat transfer, and consequently, an optimum design of a TES unit. Thus, the present research aims to address the advantage of using nano-additives in a geometrically optimum design.

2. Methodology

Fig. 1 depicts the schematic configuration of a heat exchanger energy storage system. As the schematic view illustrates, the system includes a shell and a U-shaped tube containing the hot heat transfer fluid (HTF). As can be seen in Fig. 1b, the cross-section of the tube is a quasi-petal. The tube is relatively thin and thermally conductive; therefore, its thickness is negligible compared to the radius. Moreover, the convection heat transfer inside the tube is strong, and hence, the tube was modeled as a hot isotherm surface. The shell of the heat exchanger storage system is well insulated, while the tube has high and low temperatures of $T_h = 42\ ^\circ C$ and $T_c = 22\ ^\circ C$ during the charging process. Since the cross-section of the heat exchanger energy storage system has symmetry with respect to the vertical centerline, only half of the system is studied. The void space between the U-shaped tube and the shell is occupied by NePCM, while the host PCM is capric acid having a nominal melting point of $T_f = 32\ ^\circ C$. The dispersed nano-additives can be composed of copper (Cu) or graphene oxide (GO). It is assumed that the nano-additives are homogeneously dispersed in the host PCM. Due to the nanoscale of particles, the synthesized NePCM is stable and uniform. The nanoparticles are spherical, and there is no sedimentation and agglomeration in the PCM. The thermophysical properties of all the components of the NePCM are listed in Table 1. Herein, the density variations of the NePCM during a phase change are considered to be zero, and the reference densities are selected to simulate the process. The geometry of the cross-section of the quasi-petal heat pipe is defined by using the following relation:

$$x(s) = (r_b + A \times \sin(\lambda s + \phi_0)) \times \cos\left(s + \phi_0 + \left(\frac{3\pi}{2\lambda} - \frac{\phi_0}{\lambda}\right)\right) \quad (1a)$$

$$y(s) = (r_b + A \times \sin(\lambda s + \phi_0)) \times sin\left(s + \phi_0 + \left(\frac{3\pi}{2\lambda} - \frac{\phi_0}{\lambda}\right)\right) \quad (1b)$$

The geometrical parameters r_b, A, λ, s, and ϕ_0 are shown in Fig. 1d. In this study, it is worth noting that the area of the quasi-petal heating tube, i.e., A_p, is considered to be constant and known as a constraint. It is

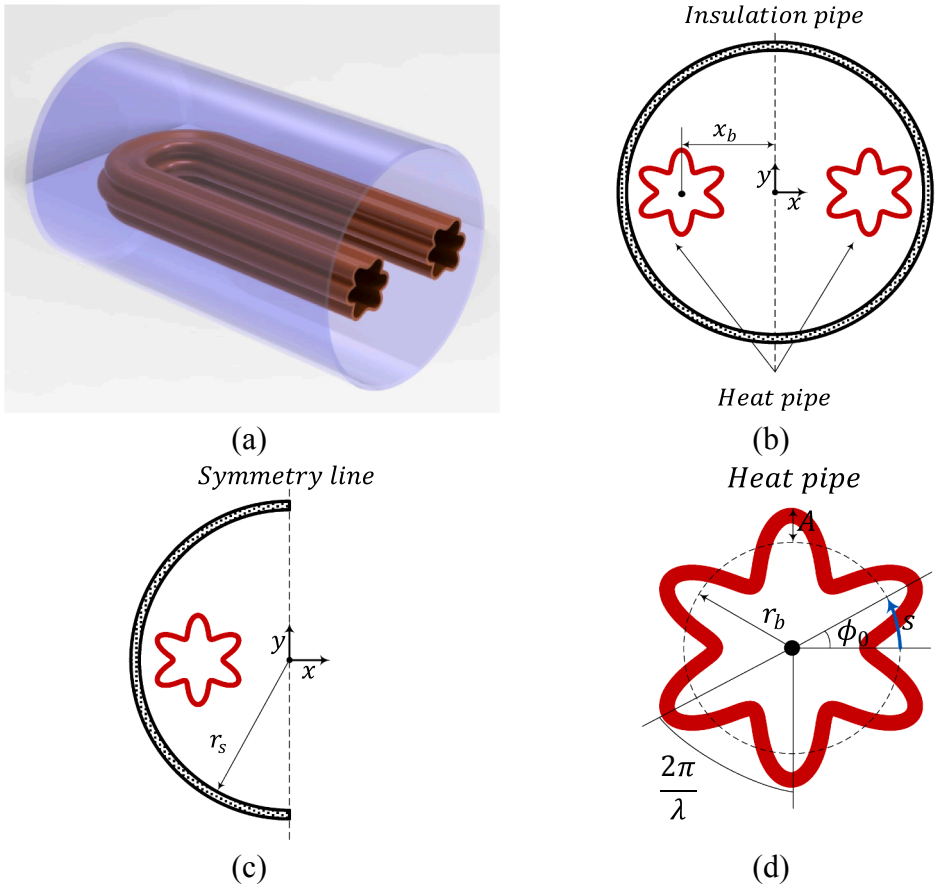

Fig. 1. Schematic view of the problem physics.

Table 1
. Thermophysical properties of the paraffin wax and the nano-additives .[28,29]

Properties	Cu nano-additives	GO nano-additives	Capric acid
Thermal conductivity ($Wm^{-1}\ K^{-1}$)	401	5000	Solid: 0.372 Liquid: 0.153
Latent heat ($kJ\ kg^{-1}$)	NA	NA	152.7
Thermal expansion coefficient (K^{-1})	1.67×10^{-5}	28.4×10^{-5}	1×10^{-3}
Fusion temperature (°C)	NA	NA	32
Density ($kg\ m^{-3}$)	8933	1800	Solid: 1018 Liquid: 888
Specific heat ($kJ\ kg^{-1}\ K^{-1}$)	0.385	0.717	Solid: 1.9 Liquid: 2.4
Kinematic viscosity ($m^2\ s^{-1}$)	NA	NA	3×10^{-6}

NA: Not applicable.

known that the surface area of the quasi-petal heat pipe is not dependent on the variables λ and A. Table 2 presents the geometrical dimensions of the cross-section of the energy storage system.

2.1. Governing equations

The governing equations representing the conservation of mass, momentum, and energy in the heat exchanger is presented as:

$$\frac{\partial u}{\partial x}+\frac{\partial v}{\partial y}=0 \tag{2}$$

Table 2
Geometrical dimensions of the cross-section of the energy storage system.

Characteristic	Value
Shell radius of the heat exchanger; r_s	Constant: $r_s = 20mm$
Surface area of the quasi-petal heated tube; A_p	Constant; $A_p = \pi r_s^2/10$
The radius of base circle making the quasi-petal heat pipe; r_b	Dependent variable; $r_b = A_p/\pi - A^2/2$
Frequency; λ	Variable
Distance of the centers of the heat pipe and shell; x_b	Variable
Deviation from the radius of the base circle; A	Variable
Rotation angle of the quasi-petal heat pipe; ϕ_0	Variable

$$\rho_{NePCM,l}\left(\frac{\partial u}{\partial t}+u\frac{\partial u}{\partial x}+v\frac{\partial u}{\partial y}\right)=-\frac{\partial p}{\partial x}+\mu_{NePCM}\left(\frac{\partial^2 u}{\partial x^2}+\frac{\partial^2 u}{\partial y^2}\right)-f(T)u \tag{3}$$

$$\rho_{NePCM,l}\left(\frac{\partial v}{\partial t}+u\frac{\partial v}{\partial x}+v\frac{\partial v}{\partial y}\right)=-\frac{\partial p}{\partial y}+\mu_{NePCM}\left(\frac{\partial^2 v}{\partial x^2}+\frac{\partial^2 v}{\partial y^2}\right)-f(T)v+(\rho\beta)_{NePCM,l}g(T-T_m) \tag{4}$$

$$(\rho C_p)_{NePCM}\left(\frac{\partial T}{\partial t}+u\frac{\partial T}{\partial x}+v\frac{\partial T}{\partial y}\right)=\frac{\partial}{\partial x}\left(\kappa_{NePCM}\frac{\partial T}{\partial x}\right)+\frac{\partial}{\partial y}\left(\kappa_{NePCM}\frac{\partial T}{\partial y}\right)-E(T) \tag{5}$$

$f(T)$, as the function of the liquid fraction of the NePCM, i.e., χ, is the momentum sink term, which is defined by using the Kozeny-Carman model.

$$f(T) = \varepsilon \frac{(1-\chi(T))^2}{\chi(T)^3 + \xi} \tag{6}$$

It is evident this term will be zero and infinity for the completely melted zone and the solid zone, respectively. ε is the mushy zone constant, and it represents the approximate magnitude of dampening in the momentum equations. This constant is set to 10^5. Likewise, ξ is set to a very low value to prevent division by zero at the melted zone. The liquid fraction of the NePCM, which is defined by the temperature, is:

$$\chi(T) = \begin{cases} 0 & T < T_m - \dfrac{\delta T}{2} \\ \dfrac{T - T_m}{\delta T} + \dfrac{1}{2} & T_m - \dfrac{\delta T}{2} < T < T_m + \dfrac{\delta T}{2} \\ 1 & T > T_m + \dfrac{\delta T}{2} \end{cases} \tag{7}$$

where T_m is the melting temperature, and δT is the melting temperature window. The energy source term is defined as the following:

$$E(T) = (\rho h_{sf})_{NePCM} \frac{\partial \chi(T)}{\partial t} \tag{8}$$

$$\text{Charing power} = \frac{\text{The amount of the energy when the melting process complete}}{\text{complete melting time}} \tag{16}$$

The density of NePCM can be calculated using the following equations:

$$\rho_{NePCM} = (1-\omega_{vf})\rho_{PCM} + \omega_{vf}\rho_{na} \tag{9a}$$

$$\rho_{PCM}(T) = \rho_{PCM,l}\chi(T) + (1-\chi(T))\rho_{PCM,s} \tag{9b}$$

where, ω_{vf} is the volumetric concentration of nanoparticles. As previously expressed, the nano-sized additives are in sphere shape. Hence, the dynamic viscosity can be defined by using the Brinkman model [30] as the following:

$$\mu_{NePCM} = \frac{\mu_{PCM}}{(1-\omega_{vf})^{2.5}} \tag{10}$$

The effective thermal conductivity of the NePCM is calculated by the following equation:

$$\kappa_{NePCM}(T) = \kappa_{NePCM,l}\chi(T) + (1-\chi(T))\kappa_{NePCM,s} \tag{11a}$$

The Maxwell model [31] is used to asses the effective thermal conductivity of the NePCM containing the spherical nano-additives as follows:

$$\frac{\kappa_{NePCM,i}}{\kappa_{PCM,i}} = \frac{(\kappa_{na} + 2\kappa_{PCM,i}) - 2\omega_{vf}(\kappa_{PCM,i} - \kappa_{na})}{(\kappa_{na} + 2\kappa_{PCM,i}) + \omega_{vf}(\kappa_{PCM,i} - \kappa_{na})} \tag{11b}$$

where i denotes the phase of the PCM, which can be l (liquid) or s (solid). The thermal-volume expansion coefficient are determined as follows:

$$(\rho\beta)_{NePCM,l} = \left[(1-\omega_{vf})(\rho\beta)_{PCM,l} + \omega_{vf}(\rho\beta)_{na}\right] \tag{12}$$

In addition, the effective heat capacity of the NePCM can ascertained using the following equations:

$$(\rho C_p)_{NePCM} = \left[(1-\omega_{vf})(\rho C_p)_{PCM} + \omega_{vf}(\rho C_p)_{na}\right] \tag{13a}$$

$$(\rho C_p)_{PCM}(T) = (\rho C_p)_{PCM,l}\chi(T) + (1-\chi(T))(\rho C_p)_{PCM,s} \tag{13b}$$

Finally, the NePCM effective latent heat can be determined using Eq. (14).

$$(\rho h_{sf})_{NePCM} = (1-\omega_{vf})\rho_{PCM} h_{sf,PCM} \tag{14}$$

The total energy accumulated in the system, which involves both sensible and latent energies, is given by:

$$ES = \int_A \int_{T_{in}}^{T_s} (\rho C_p)_{NePCM,s} dT dA + \int_A (\rho h_{sf})_{NePCM} dA + \int_A \int_{T_l}^{T} (\rho C_p)_{NePCM,l} dT dA \tag{15}$$

Initially, at $t = 0$, the temperatures of the NePCM and the quasi-petal heat pipe are T_c. At $t = 24$ s, the temperature of the heat pipe linearly rises until it reaches T_h at $t = 25$ s. As previously mentioned, the outer shell of the system is well insulated.

The performance of energy storage can be described by charging power. This parameter shows the capacity of the PCM to store energy, and it is dependent upon on the amount of the energy stored at 100% melting volume fraction:

3. Numerical method

To simulate the melting process, source terms should be included in the momentum and energy equations. The source terms in the momentum equations $u f(T)$ and $v f(T)$ are considered to control the velocity field as the phase of the material changes from solid to liquid. The three regions that may exist in the phase change material are the melted region, the non-melted region and the interstitial region between them, which is the mushy zone. These regions can be distinguished from one another based on the fusion temperature and the melting temperature window, which is denoted as δT. High velocity and temperature gradients exist in the mushy zone region, which requires the use of a high-quality mesh with high resolution. To decrease the computational cost, the finer grids should only be adopted for the mushy zone region. During the melting process, the mushy zone is in constant flux relative to its size, shape, and location; therefore, the mesh adaption technique should be implemented to capture this region.

The described governing equations are solved using a finite element-based Galerkin algorithm. Using this technique, the governing equations, along with the boundary and initial conditions, are transferred into a new form, which is referred to as the weak form. A shape set expressed by $\{z_j\}_{j=1}^{N}$ is implemented to expand the governing dependent variables, i.e., u, v, T, and p.

$$(u, v, p, T) \approx \sum_{j=1}^{N} (u_j, v_j, p_j, T_j) z_j(x,\ y) \tag{17}$$

By using the Galerkin finite element method, the set of governing equations were rewritten in the form of discrete residuals at each computational element as:

$$Q_n^1 \approx \sum_{N}^{j=1} u_j \int \frac{\partial z_j}{\partial x} z_n dx dy + \sum_{N}^{j=1} v_j \int \frac{\partial z_j}{\partial y} z_n dx dy \tag{18a}$$

$$Q_n^2 \approx \rho_{NePCM,l}\sum_{j=1}^{N} u_j \int \frac{\partial z_j}{\partial t} z_n dxdy + \rho_{NePCM,l}\sum_{j=1}^{N} u_j \int \left[\left(\sum_{j=1}^{N} u_j z_j\right)\frac{\partial z_j}{\partial x} + \left(\sum_{k=1}^{N} v_j z_j\right)\frac{\partial z_j}{\partial y}\right] z_n dxdy + \sum_{j=1}^{N}\int\left(-\sum_{j=1}^{N} p_j z_j\right)\frac{\partial z_j}{\partial x} z_n dxdy + \mu_{NePCM}\sum_{j=1}^{N} u_j \int \frac{\partial z_j}{\partial x}\frac{\partial z_i}{\partial x} dxdy + \mu_{NePCM}\sum_{j=1}^{N} u_j \int \left[\frac{\partial z_j}{\partial y}\frac{\partial z_i}{\partial y}\right] dxdy - \mu_{NePCM}\int\left(\sum_{j=1}^{N} u_j z_j\right) z_n dxdy - f(T)\int\left(\sum_{j=1}^{N} u_j z_j\right) z_n dxdy \quad (18b)$$

$$Q_n^3 \approx \rho_{NePCM,l}\sum_{j=1}^{N} v_j \int \frac{\partial z_j}{\partial t} z_n dxdy + \rho_{NePCM,l}\sum_{j=1}^{N} v_j \int \left[\left(\sum_{j=1}^{N} u_j z_j\right)\frac{\partial z_j}{\partial x} + \left(\sum_{j=1}^{N} v_j z_j\right)\frac{\partial z_j}{\partial y}\right] z_n dxdy + \sum_{j=1}^{N}\int\left(-\sum_{j=1}^{N} p_j z_j\right)\frac{\partial z_j}{\partial y} z_n dxdy + \mu_{NePCM}\sum_{j=1}^{N} v_j \int \frac{\partial z_j}{\partial x}\frac{\partial z_n}{\partial x} dxdy + \mu_{NePCM}\sum_{j=1}^{N} v_j \int \left[\frac{\partial z_j}{\partial y}\frac{\partial z_n}{\partial y}\right] dxdy - \mu_{NePCM}\int\left(\sum_{j=1}^{N} v_j z_j\right) z_n dxdy - f(T)\int\left(\sum_{j=1}^{N} v_j z_j\right) z_n dxdy + (\rho\beta)_{NePCM,l} g\left(\int\left(\sum_{j=1}^{N} T_j z_j\right) z_n dxdy - T_m\right) \quad (18c)$$

$$Q_n^4 \approx (\rho C_p)_{NePCM}\sum_{j=1}^{N} T_j \int \frac{\partial z_j}{\partial t} z_n dxdy + (\rho C_p)_{NePCM}\sum_{j=1}^{N} T_j \int \left[\left(\sum_{j=1}^{N} u_j z_j\right)\frac{\partial z_j}{\partial x} + \left(\sum_{j=1}^{N} v_j z_j\right)\frac{\partial z_j}{\partial y}\right] z_n dxdy + k_{NePCM}\sum_{j=1}^{N} T_j \int \left[\frac{\partial z_j}{\partial x}\frac{\partial z_n}{\partial x} + \frac{\partial z_j}{\partial y}\frac{\partial z_n}{\partial y}\right] dxdy - (\rho h)_{NePCM}\sum_{j=1}^{N}\frac{\partial \chi(T)}{\partial T}\int \frac{\partial z_j}{\partial t} z_n dxdy \quad (18d)$$

where

$$\frac{\partial \chi(T)}{\partial T} = \begin{cases} 0 & T \leqslant T_m - \frac{1}{2}\delta T \\ \frac{1}{\delta T} & T_m - \frac{1}{2}\delta T < T < T_m + \frac{1}{2}\delta T \\ 0 & T \geqslant T_m + \frac{1}{2}\delta T \end{cases} \quad (19)$$

The integral of the above residual equations is computed numerically utilizing the second-order Gaussian-quadrature approach. The details of the finite element numerical method, as based on the Galerkin technique, can be found in detail in [32,33].

A modified phase-field variable χ_0 is introduced to distinguish the mesh adaptation zone, where $\chi_0 = 1$ means that mesh adaptation is applied to this domain. The phase change hypothetically takes place at a relatively extended temperature interval of $3\delta T/2$ rather than δT. This slightly wider phase change temperature interval leads to a slightly wider region around the actual phase change domain. Such a region permits for smoother mesh transition at the phase change interfacial region. The mesh adaptation, which applies to the extended region around the transition interface, leads to a very fine mesh. The mesh in the $\chi_0 = 1$ region is fivefold finer compared to the typical domain meshes. Here, $\chi_0 = 1$ is defined as:

$$\chi_0(T) = \begin{cases} 0 & T \leqslant T_m - \frac{3}{2}\delta T \\ 1 & T_m - \frac{3}{2}\delta T < T < T_m + \frac{3}{2}\delta T \\ 0 & T \geqslant T_m + \frac{3}{2}\delta T \end{cases} \quad (20)$$

The generated grid is appropriate for the calculation, while the mushy zone variability stays within the adapted domain. Therefore, considering an adapted region that is slightly larger than the phase change region reduces the quantity of grid reconfigurations. It should be noted that employing the adaptive mesh procedure on large domains results in a large number of mesh elements. Consequentially, this results in increased computational costs, so it is always recommended to use relatively large mesh adaptation domains, especially at the intermediate time steps. Thus, the employed approach is computationally effective.

To discretize the time-dependent terms in the governing equation, a time adaptation technique based on the Backward Differentiation Formula (BDF) was employed [34]. The Newton method iterative solver (damping factor of 0.8) was applied for the solution of the residual equations of Eq. (18). The iterations were implemented with a residual error O(10^{-6}) by using a PARallel DIrect SOlver (PARDISO) [35–37].

3.1. Grid check

It is important that the gird size and the obtained numerical results are not dependent on one another; therefore, six different grids were considered as presented in Table 3. Adaptive grid refinement was applied for each case, as shown in Fig. 2. The following geometrical dimensions were chosen for the mesh independency study: $\omega_{vf} = 0.08$, $x_b = 0.375 \times r_s$, $A = 0.15 \times r_s$ and $\lambda = 8$. The results for the average shell temperature and the energy stored are reported in Table 3. In addition, the time variation of the liquid fraction and the stored energy are displayed in Figs. 3 and 4. To further investigate the effect of the grid size on the melting process, the solid-liquid interface is also shown in Fig. 5 for the selected grid sizes. It can be seen that as the number of elements increases, the variations between the results decreases. The obtained results suggest that the grid with 4988 elements (Case III) is sufficiently small and is adequate for all the computations.

3.2. Validation and verification

For verifying the accuracy of the numerical model and validating the obtained results, some comparisons are conducted between the results of the current study and to those available in the literature. The first comparison is performed using the experimental data available by Kumar et al. [38]. In the experimental study by Kumar, the progress of the phase-change interface during the lead melting process was observed utilizing neutron radiography [36]. All container walls were isolated, except for the vertical side-wall, which was subjected to a constant heat flux. Fig. 6 illustrates the comparison of the melting front obtained from the current study to those of Kumar et al. [38] for an applied heat flux of 16.3 kW/m^2 and at different time snaps when $Ra =$

Table 3
Different mesh sizes at the end of the process for Cu-nanoparticles with $\omega_{vf} = 0.08$, $x_b = 0.375 \times r_s$, $A = 0.15 \times r_s$ and $\lambda = 8$ values (Case III was chosen as the mesh independency).

Case study	Number of elements	Shell average temperature [K]	*ES* [J/m]
Case I	3487	314.14	91,703
Case II	4067	314.04	91,914
Case III	4988	313.99	91,918
Case IV	6012	313.97	91,934
Case V	8376	313.95	91,955
Case VI	9031	313.95	91,969

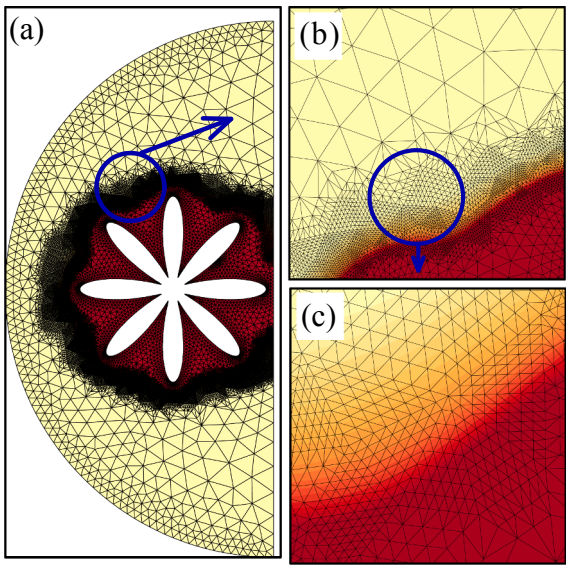

Fig. 2. Utilized case III mesh grid at $t = 200$ s.

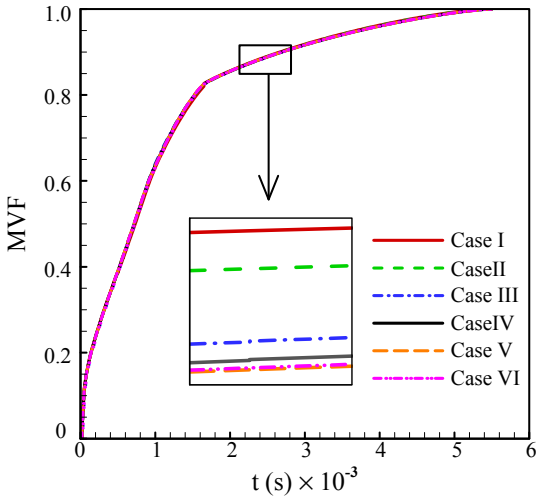

Fig. 3. *MVF* as a function of time for different mesh sizes ($\omega_{vf} = 0.08$, $x_b = 0.375 \times r_s$, $A = 0.15 \times r_s$ and $\lambda = 8$).

1.4×10^7, $Ste = 0.4$, and $Pr = 0.0236$. As displayed in Fig. 6, a strong agreement was obtained with regard to the shape and the extent of the molten region.

For the second comparison, the present melt front results are compared to the results reported by Bertrand et al. [39] where the melting of a base PCM inside a cavity was studied. The horizontal walls of the enclosure were isolated, while both vertical left and right walls were heated and cooled, respectively. The values of the considered study parameters were set as $Pr = 50$ and $Ra = 1.25 \times 10^5$, while $Fo.\,Ste = 0.01$ and $Fo.\,Ste = 0.002$ were adopted for comparisons. As it can be observed in Fig. 7, the currently obtained results show good agreement with those available in the literature.

In addition to the previously mentioned validations, the results are also compared to those available by Kuehn and Goldstein [40] to evaluate the natural convection heat transfer. The natural convection heat transfer in the annulus was studied where air and water were used as the filling fluid. The ratio of the gap width of the annulus (L) to the inner cylinder diameter (D_i) was selected as 8 ($L/D_i = 0.8$). The isotherm contours obtained from the current works are depicted versus the experimentally obtained isotherms by Kuehn and Goldstein [40] in

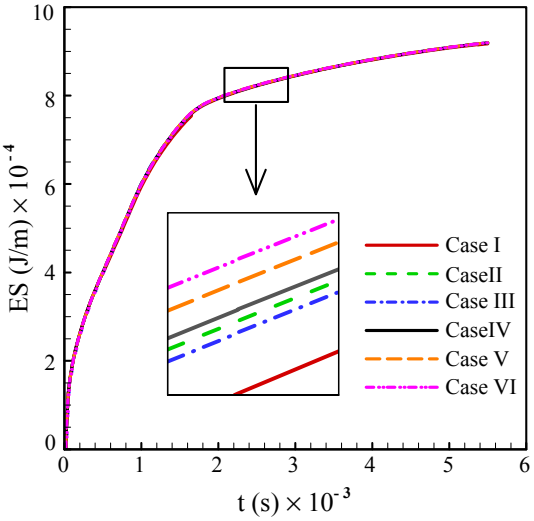

Fig. 4. Total energy as a function of time for different mesh case studies ($\omega_{vf} = 0.08$, $x_b = 0.375 \times r_s$, $A = 0.15 \times r_s$ and $\lambda = 8$).

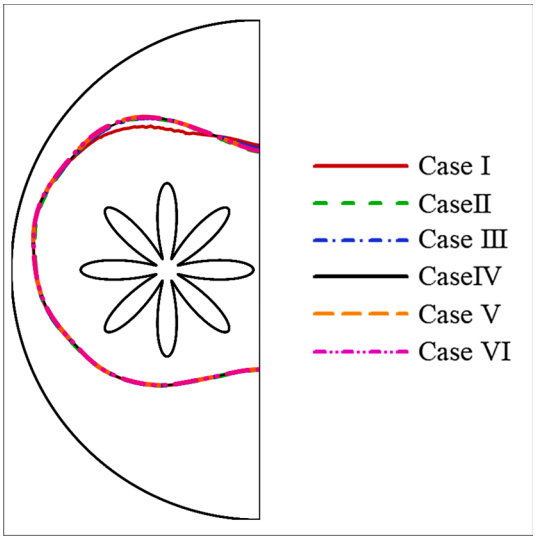

Fig. 5. The solid-liquid interface for different mesh grid at $t = 700$ s ($\omega_{vf} = 0.08$, $x_b = 0.375 \times r_s$, $A = 0.15 \times r_s$ and $\lambda = 8$).

Fig. 8. The Prandtl and Reynolds numbers are considered to be 0.706 and 4.7×10^4, respectively. As can be inferred from Fig. 8, a very good agreement is obtained.

4. Results and discussion

The effects of key parameters, such as the distance of the centers of the heat pipe and shell (x_b), the amplitude of deviation from the base circle (A), frequency (λ), and nanoparticle volume concentration (ω_{vf}) are investigated on the performance of the system. The following ranges are considered for each variable in the current study: $0.375r_s \le x_b \le 0.625r_s$, $0 \le A \le 0.15r_s$, $2 \le \lambda \le 8$, and $0.0\% \le \omega_{vf} \le 8\%$.

4.1. Optimization

This section discusses the application of the previously described Taguchi experimental design method for the optimization of the heat exchanger energy storage system, which was depicted in Fig. 1. The Taguchi design method is a powerful statistical technique utilized for

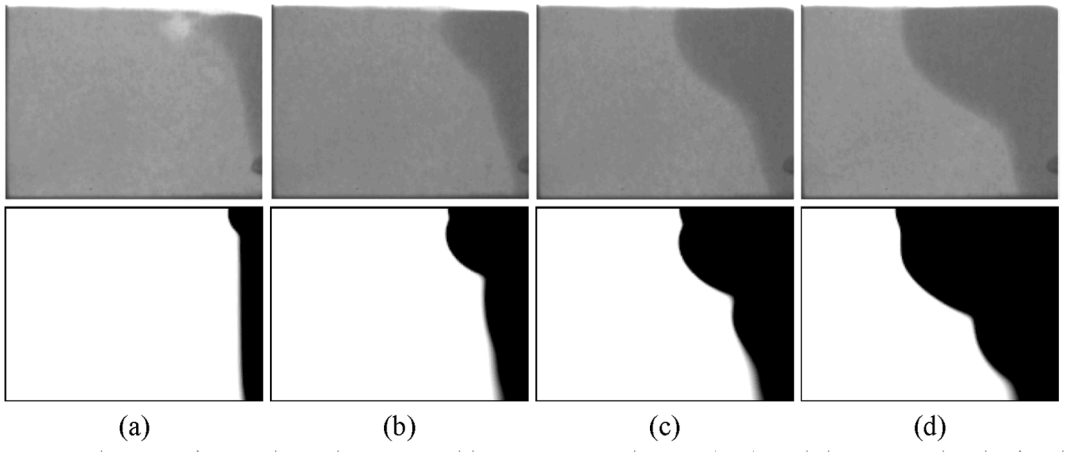

Fig. 6. The experimental results reported by Kumar et al. [38] (top) and the currently obtained numerical results (bottom) at various time snaps of (a): 139 s, (b): 277 s, (c): 416 s, and (d): 554 s.

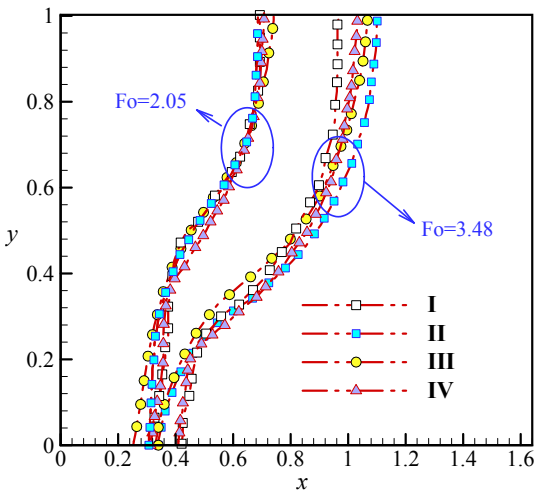

Fig. 7. A comparison of the currently obtained results against the literature review of [39] I: Kashani et al. [41] II: Gau and Viskanta (experiment); III: Brent et al., and VI: present work.

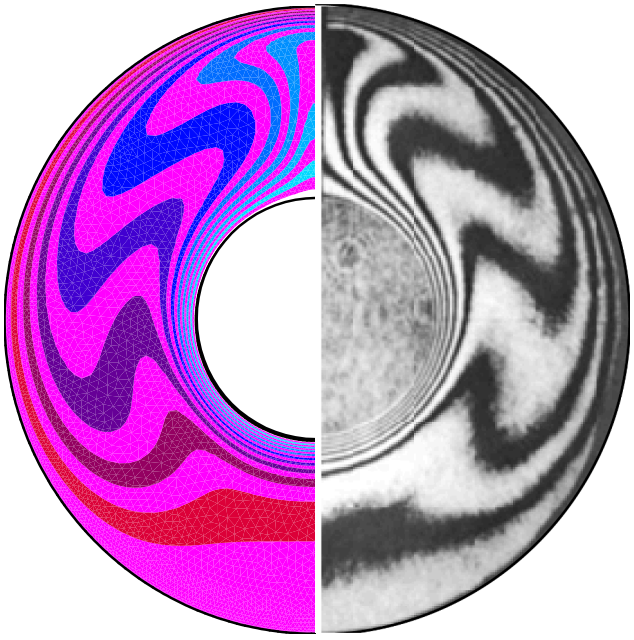

Fig. 8. Comparison of the currently obtained isotherm (left) against Kuehn and Goldstein [40] (right).

optimizing process parameters. The significant advantage of the Taguchi method is the effective estimation of process variables of an experiment to achieve optimal conditions while also minimizing the number of test runs [42]. In this regard, the concept of orthogonal arrays is used to select a suitable set of the simulation depends on the number of control factors and their levels [43]. In addition, in this method, the analysis of variance is used to investigate the influence of each parameter on the response by determining the signal-to-noise (SNR) ratio, which demonstrates the ratio of desired results (signal) to undesired results (noise) [44,45].

To plan the experiments, we select four factors with three levels, as reported in Table 4. To analyze all possible combinations, $3^4 = 81$ experiments are required. However, the Taguchi method provides similar information but decreases the number of experiments to nine through the use of the L9 orthogonal array. This reduction in the number of experiments is very helpful for the current problem with high computational cost. The orthogonal array, in conjunction with the response data (i.e., the total energy storage) for the corresponding experiments, is presented in Table 5.

In the Taguchi experimental design method, three criteria determine optimization, which are the lower-the-better, the nominal-the-better, and the higher-the-better. The optimization goal of this study is to elevate the total energy storage. Therefore, the higher-the = better

Table 4
The control factors and levels in this study.

Control factor	Levels		
	1	2	3
x_b/r_s	0.375	0.5	0.625
A/r_s	0	0.075	0.15
Λ	2	5	8
$\omega_{vf}(\%)$	0	4	8

category is selected. The signal-to-noise ratio for this case is obtained as [43]:

$$SNR = -10log\sum\frac{(1/y_n^2)}{n} \tag{21}$$

Here, y_n denotes each experiment response, while the number of experiment iterations is denoted by n. The *SNR* values for the current L9 orthogonal array are reported in Table 5. As discussed in the grid check

Table 5
The L9 orthogonal array with the response data and SNR values.

Experiment number	x_b/r_s	A/r_s	λ	ω_{vf}(%)	*ES* (J/m)		*SNR* (dB)	
					Cu	GO	Cu	GO
1	0.375	0	2	0	50,444	50,444	94.06	94.06
2	0.375	0.075	5	4	62,152	61,696	95.87	95.81
3	0.375	0.15	8	8	72,929	71,791	97.26	97.12
4	0.5	0	5	8	58,714	57,780	95.37	95.24
5	0.5	0.075	8	0	64,306	64,306	96.17	96.17
6	0.5	0.15	2	4	56,829	56,208	95.09	95.00
7	0.625	0	8	4	51,329	50,928	94.21	94.14
8	0.625	0.075	2	8	52,498	51,580	94.40	94.25
9	0.625	0.15	5	0	62,799	62,799	95.96	95.96

Table 6
The mean amounts of the SNR values for each level of the control factors.

Level	x_b/r_s		A/r_s		λ		ω_{vf}	
	Cu	GO	Cu	GO	Cu	GO	Cu	GO
1	95.73	95.66	94.55	94.48	94.52	94.43	95.39	95.39
2	95.54	95.47	95.48	95.41	95.73	95.67	95.06	94.98
3	94.86	94.78	96.10	96.03	95.88	95.81	95.68	95.54
Delta	0.87	0.88	1.56	1.55	1.36	1.37	0.62	0.56
Rank	3		1		2		4	

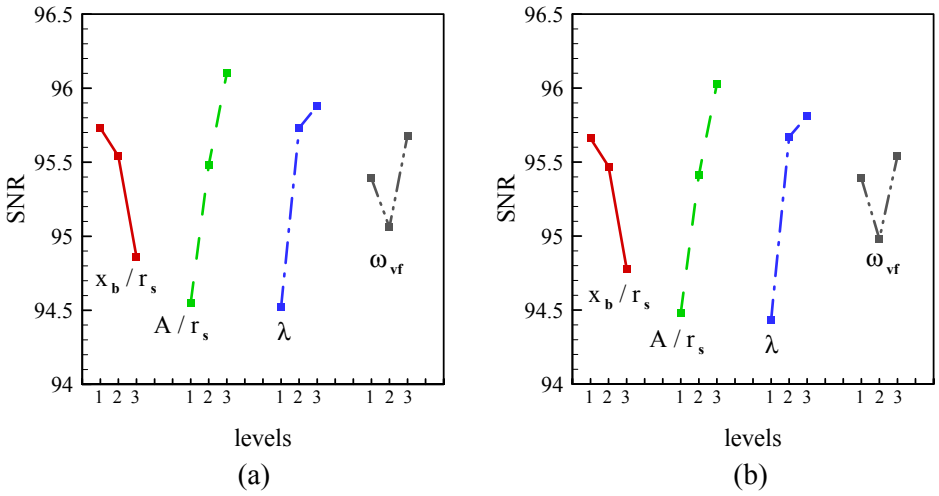

Fig. 9. Plots of the mean amounts of SNR: (a) Cu and (b) GO.

section, the following parameters were chosen as the reference condition of the problem; $\omega_{vf} = 0.08$, $x_b = 0.375 \times r_s$, $A = 0.15 \times r_s$ and $\lambda = 8$. The total energy storage was calculated for reference parameters when the melting volume fraction reached 0.75 in 1400 s.

The 1400 s was considered as a criterion to study the influence of the previously mentioned parameters on total energy storage show in Table. 5. Thus, the data of Table 5 shows the stored energy at $t = 1400$ s. The unit of energy shows the stored energy per length of the TES.

Table 6 and Fig. 9 provide mean values of the *SNR* associated with each respective control factor level. Here, the optimum level for each factor is acquired by selecting the level having the highest value of *SNR*. Therefore, the optimum combination of the factors and levels leading to the highest value of the total energy storage is: $x_b/r_s = 0.375$, $A/r_s = 0.15$, $\lambda = 8$, and $\omega_{vf} = 8\%$ which is case 3 of Table 5. The average amount of stored energy for all nine cases of Table 5 is 59.111 kJ/m for Cu and 58.615 kJ/m for GO NePCM after 1400 s of thermal charging. A comparison between these average values and the optimum case shows 23.3% (Cu) and 22.5% (GO) improvement of stored thermal energy during the 1400 s. The improvement present was computed as 100 × (*ES* for case 3 - average *ES*)/ average *ES*. These improvements clearly indicate the suitability for the optimum design in the current heat exchanger energy storage system. Table 5 also shows that the copper nano-additives are more effective than the graphene oxide nano-additives in all cases. Moreover, Case 1 represents a design for a circular tube with no nanoparticles. A comparison between this case and Case 3 (optimum case) shows 45% improvement, 100 × (*ES* for Case 3 – *ES* for Case 1)/(*ES* for Case 1).

In Table 6, the delta value for each factor shows the discrepancies that appear between the *SNR* maximum and minimum values. This definition implies that a higher delta value equates to a stronger influence; therefore, we can rank the control factors according to their role. It should be noticed that in Table 6, the order of the factor effectiveness is: $A/r_s > \lambda > x_b/r_s > \omega_{vf}$. This indicates that the influence of the nano-additives is weaker than the geometric parameters of the heat exchanger energy storage system.

Now, an analysis of variance (ANOVA) is applied to the results of the Taguchi method to determine the contribution ratio of the current control factors. In this method, the degree of freedom for each control

Table 7
ANOVA results for two nanoparticles of Cu and GO.

Control factor	Degree of freedom	Sum of squares		Variance		Contribution ratio	
		Cu	GO	Cu	GO	Cu	GO
x_b/r_s	2	1.27	1.28	0.63	0.64	14.25	14.42
A/r_s	2	3.68	3.65	1.84	1.82	41.46	41.19
λ	2	3.35	3.43	1.68	1.71	37.73	38.75
ω_{vf}	2	0.58	0.50	0.29	0.25	6.56	5.65
Total	8	8.88	8.85				

factor is defined as the number of levels of that factor in the orthogonal arrays minus 1. Meanwhile, the variance of a factor is obtained by dividing the sum of squares by the degree of freedom. This parameter represents how the response of a system depends on that factor in a way that a factor with a larger variance has higher effectiveness. Additionally, the contribution ratio of a controlling factor is computed as the ratio of the sum of the squares of that factor to the sum of the squares of all factors. The results of the ANOVA are presented in Table 7. Here, the order of the effectiveness of the control factors confirms the outcomes of the Taguchi method. Notice that A/r_s has a dominant influence on the total energy storage with a contribution ratio of about 41%. Next, λ contributes about 41%. The sum of contribution ratios of these two factors is more than 79%. Meanwhile, the factor effectiveness of x_b/r_s and ω_{vf} are about 14% and 5–6%, respectively.

4.2. Fundamental analysis

The temperature contours, melting volume fraction contours, and streamlines at various times are illustrated in Fig. 10. The considered case uses a heated tube with a frequency of eight ($\lambda = 8$). The copper nanoparticles with an 8% volume fraction are selected, and x_b and A are set at $0.375r_s$ and $0.15r_s$, respectively. As illustrated by the figures, in the beginning, the melting process is limited to the layers surrounding the heated tube. At this phase, the heat transfer process is mainly controlled by conduction heat transfer; however, natural convection vortices develop between the tube petals.

As the melting process continues, more PCM changes from a solid to a liquid, and natural convection becomes stronger as it plays a more intensified role in the melting process. It can be observed that two large recirculation zones are formed in the space above the tube, which increases the melting rate at this stage. As the liquid regions extend, the two recirculation zones merge, and an additional smaller recirculation zone is formed below the tube. In general, the developed recirculation zones cause a higher melting rate at the upper half of the container. As time passes, a thick layer of liquid covers the heat transfer source, and the temperature difference between the PCM layers and the heat transfer source decreases. At $t > 2000s$, the melting process is now dominated by mixed weak convection and conduction as confirmed by the horizontal isotherms, thereby causing a decrease in the melting rate.

4.2.1. Nanoparticles type and volume fraction

To evaluate the effects of nanoparticle volume fraction on the melting procedure, the melting liquid fraction is presented in Fig. 11a and Fig. 11b for Cu and GO nanoparticles, respectively. The figures show

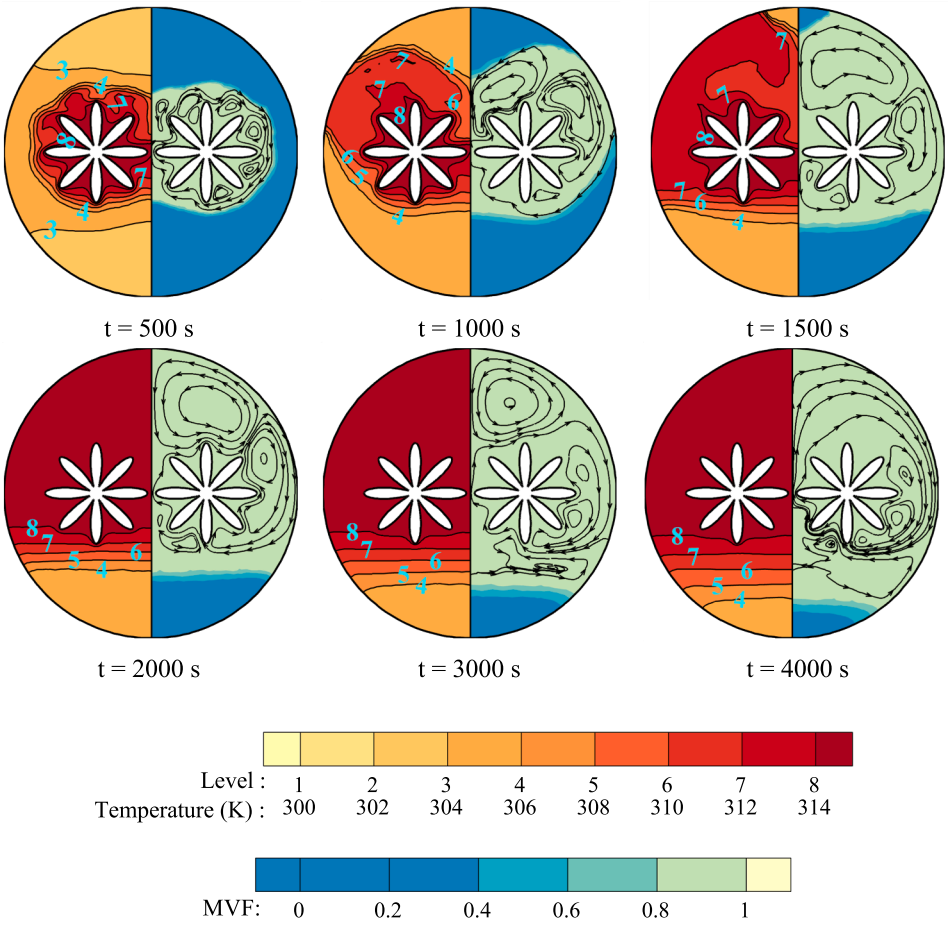

Fig. 10. The isotherms, streamlines, and melt volume fraction of the phase change with Cu nano-particles process over time: the optimum case with $\omega_{vf} = 0.08$, $x_b = 0.375 \times r_s$, $A = 0.15 \times r_s$ and $\lambda = 8$.

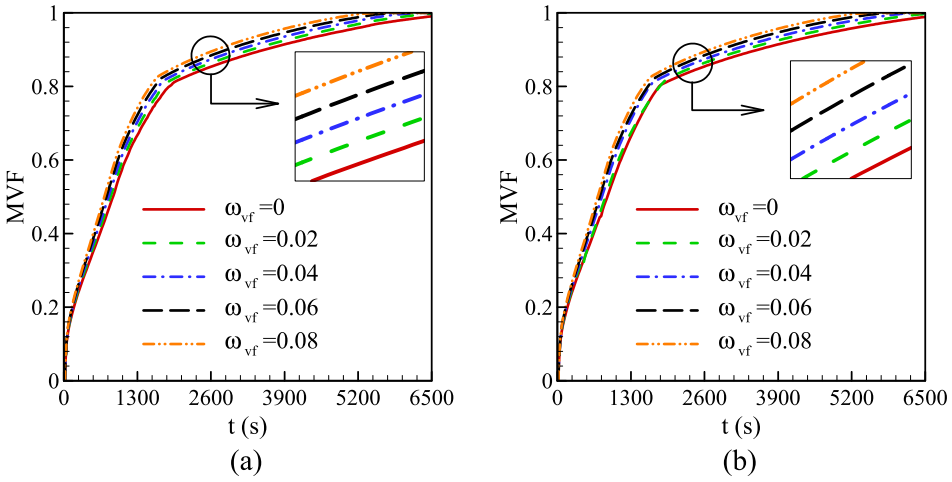

Fig. 11. Variation of *MVF* over time for (a) Cu and (b) GO nano-particles with different volume fractions ($x_b = 0.375 \times r_s, A = 0.15 \times r_s$ *and* $\lambda = 8$).

that for both nanoparticles, the pure PCM results in a slower melting rate. It is also observed that when the nanoparticle volume fraction increases, the melting process accelerates, and a higher liquid fraction is obtained.

The effects of nanoparticle volume fraction are significant in the later times of the melting. In general, the dispersion of nanoparticles within the PCM will increase the effective thermal conductivity while decreasing the latent heat of fusion, which both favorably impact the melting process. However, the inclusion of nanoparticles increases the viscosity of the NePCM, which, in turn, dampens the natural convection. This phenomenon can adversely affect the melting rate. Overall, the obtained results highlight the positive effects of nanoparticles on decreasing both the melting time and the charging time. This indicates that for the considered volume fractions, the effects of enhanced thermal conductivity and reduced latent heat should be more prominent than the increase in viscosity. Similar results are reported in an experimental study conducted by Mayilvelnathan and Valan [46]. The melting rate should not be considered as the only criterion to find the optimal case. Another important factor that should be evaluated is the stored energy as shown in Fig. 12 a and b.

The temporal variation of the stored energy shows that, in general, the amount of stored energy increases as the melting process progresses. At the initial phase of the melting process, the stored energy rate is faster as a large temperature difference exists between the heat transfer source and the solid PCM. In addition, a strong buoyancy-driven flow exists, which contributes to the rapid charging rate. The evaluation of stored energy changes with respect to a change in the nanoparticle volume fraction suggests that the presence of nanoparticles within the PCM will slightly increase the stored energy at the rapidly charging phase of the melting process. As the melting process proceeds, the increase in the nanoparticle volume fraction decreases the amount of stored energy.

In general, it should be noted that the discrepancy between the stored energies for different nanoparticle volume fractions is not noticable, especially at the beginning of the melting process. To have a closer look at the nanoparticle effects on the stored energy, the total stored energy, sensible and latent stored energy are plotted for copper nanoparticles with 2% and 8% by volume concentration in Fig. 13a, b, and c. Fig. 13b shows that the inclusion of nanoparticles in the PCM will reduce the latent storage as the PCM latent heat of fusion decreases. However, Fig. 9c reveals that the addition of nanoparticles results in higher sensible storage due to higher specific heat of the NePCM. As the latent energy makes up the bulk of the total energy, the total energy decreases with the inclusion of the nanoparticles in the PCM and with an increase of the nanoparticle volume concentration, as shown in Fig. 13a. This correlation is also noted by Akhmetov et al. [47].

Fig. 14 displays the effects of nanoparticle volume concentration on the charging power for Cu and GO nanoparticles. As previously mentioned, charging power was obtained from Eq. (15) which was the

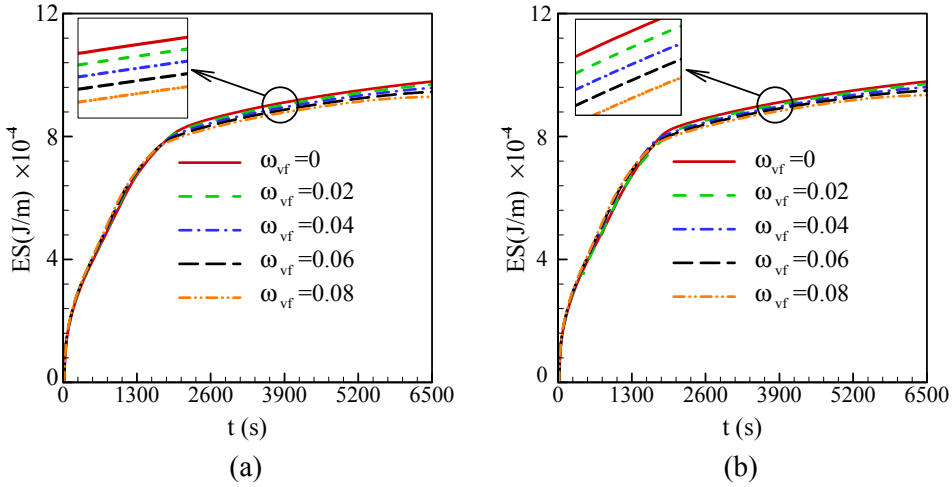

Fig. 12. Variation of total energy storage (*ES*) over time for (a) Cu and (b) GO nano-particles with different volume fractions ($x_b = 0.375 \times r_s$, $A = 0.15 \times r_s$ and $\lambda = 8$).

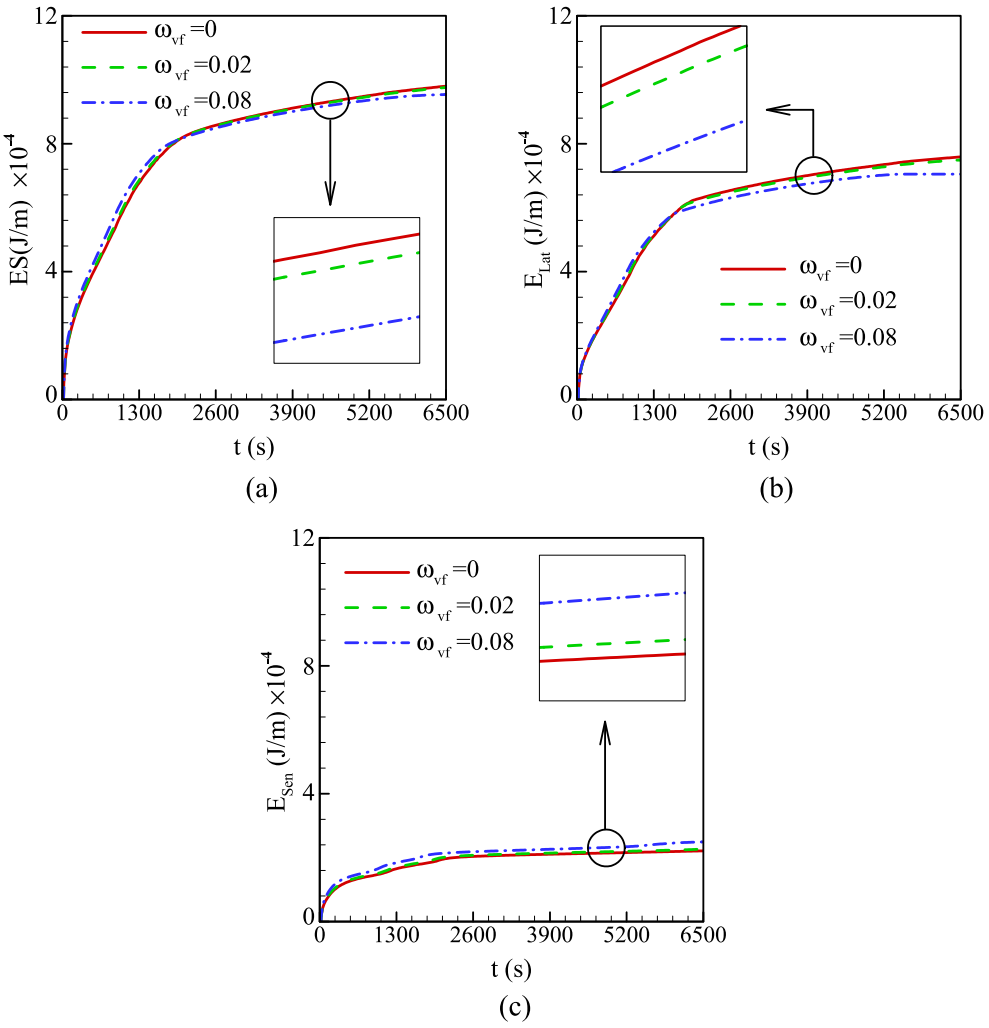

Fig. 13. Variation of (a) total energy storage (*ES*), (b) latent heat (E_{Lat}) and (c) sensible heat (E_{Sen}) over time for Cu nanoparticle with different volume fractions ($x_b = 0.375 \times r_s$, $A = 0.15 \times r_s$ and $\lambda = 8$).

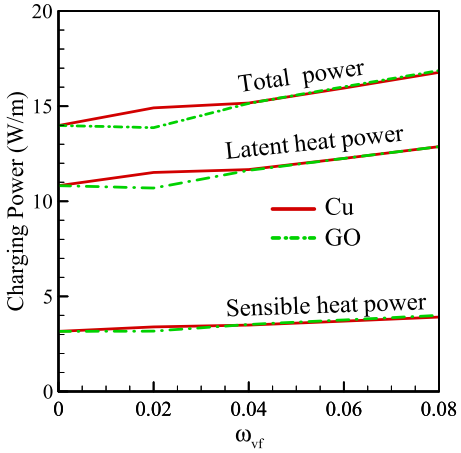

Fig. 14. Charging power against volume fraction of the Cu and GO nanoparticle ($x_b = 0.375 \times r_s$, $A = 0.15 \times r_s$ *and* $\lambda = 8$).

ratio of the total stored energy and the required time. Fig. 10 shows that the complete melting time for a process reduces when the nanoparticles' volume fraction increases, which leads to the charging power increment (Eq. (15)).

It is observed that the increase of the volume fraction of the nanoparticles increases the sensible and latent powers due to the same reason. The presence of nanoparticles could slightly reduce the amount of total energy capacity of the enclosure, but a notable reduction in the heat transfer results in an overall power enhancement. Adding nanoparticles with an 8% volume concentration will increase the total charging power by about 17%. The copper nanoparticles show higher latent and total power at lower values of nanoparticle volume concentration. The variances between the results obtained for two nanoparticle types becomes insignificant as the volume fraction increases above 4%.

The effects of the distance of the centers of the tube on the isotherms, streamlines, and liquid fraction contour is shown in Fig. 15. As seen in this figure, copper nanoparticles with an 8% volume fraction are utilized. The parameter A is set to $0.15r_s$. The progression of the PCM liquid fraction over time is also presented in Fig. 16 a. It should be noted that, in general, similar patterns are obtained at the initial phase of melting (i.e., $t = 500s$). The natural convection circulation zones are established between the petals for the three cases. As the melting processes continue, a larger natural convection circulation zone is formed in the region above the heated pipe for the case with the heated pipe located in the middle (halfway through the shell), which resulted in faster melting rates. It can be inferred that by placing the heated pipe in the middle will favor the development of the natural convection cell. For the case with the heated pipe located near the shell, the circulation zone between the heated pipe and the shell has not been able to form and the authors

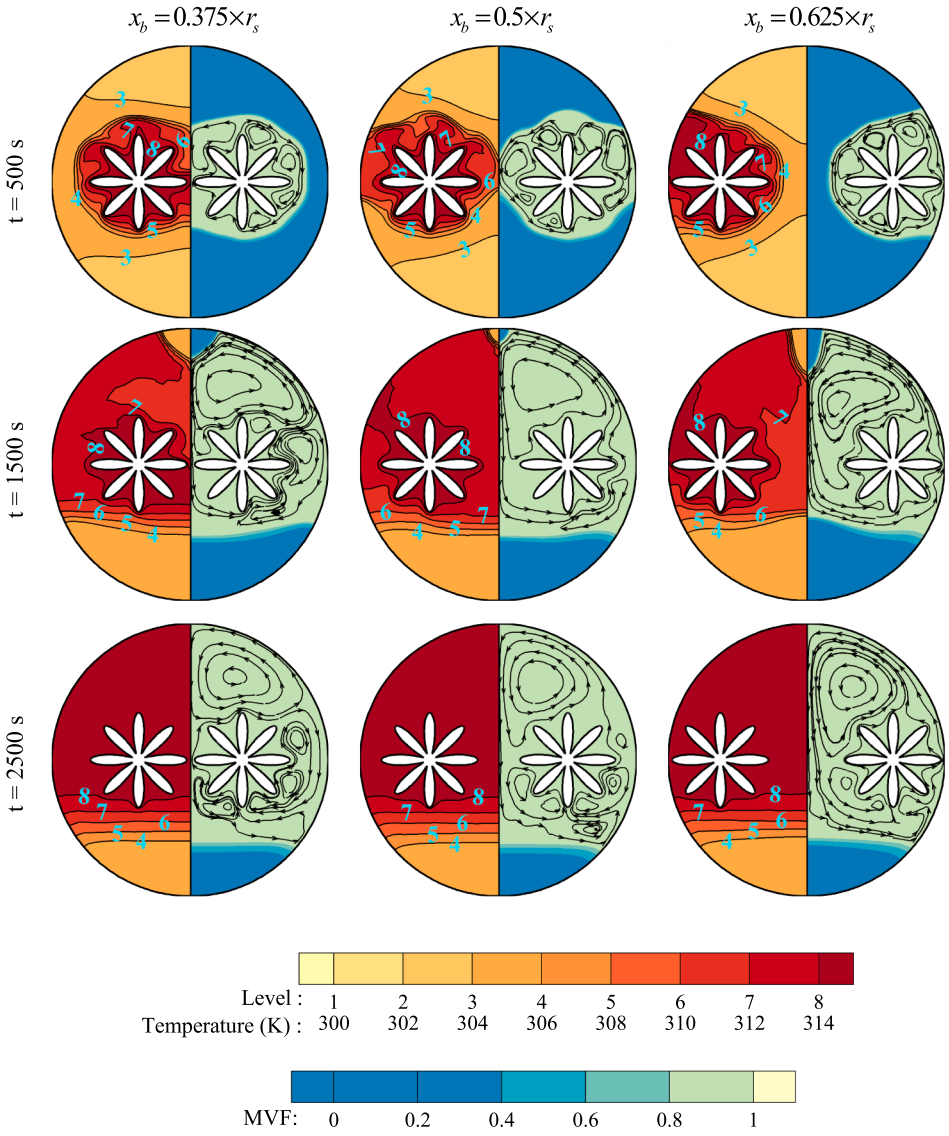

Fig. 15. The effect of the distance of the centers of the heated pipe on the isotherms, streamlines, and melting volume fraction for Cu particles with $\omega_{vf} = 0.08$, $\lambda = 8$ *and*$A = 0.15 \times r_s$.

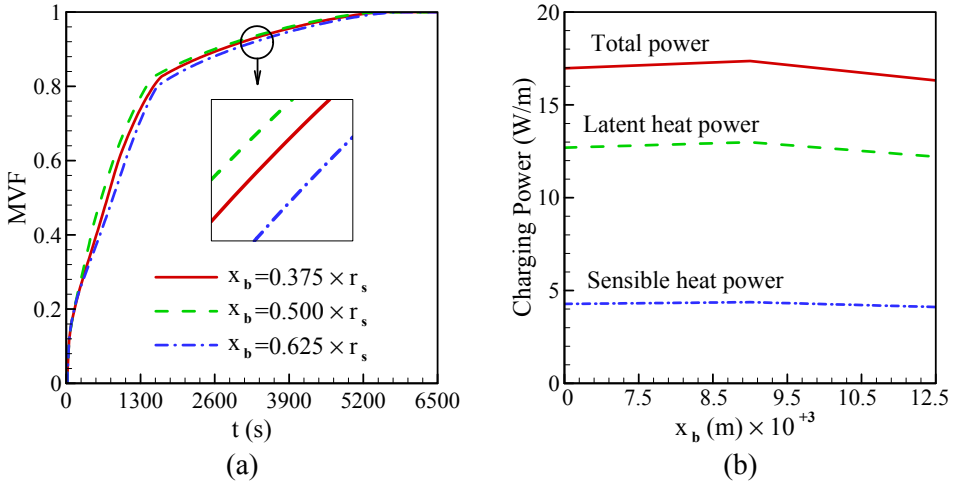

Fig. 16. Effect of x_b on (a) *MVF* and (b) the charging power for Cu nanoparticles when $\omega_{vf} = 0.08, \lambda = 8$ *and* $A = 0.15 \times r_s$.

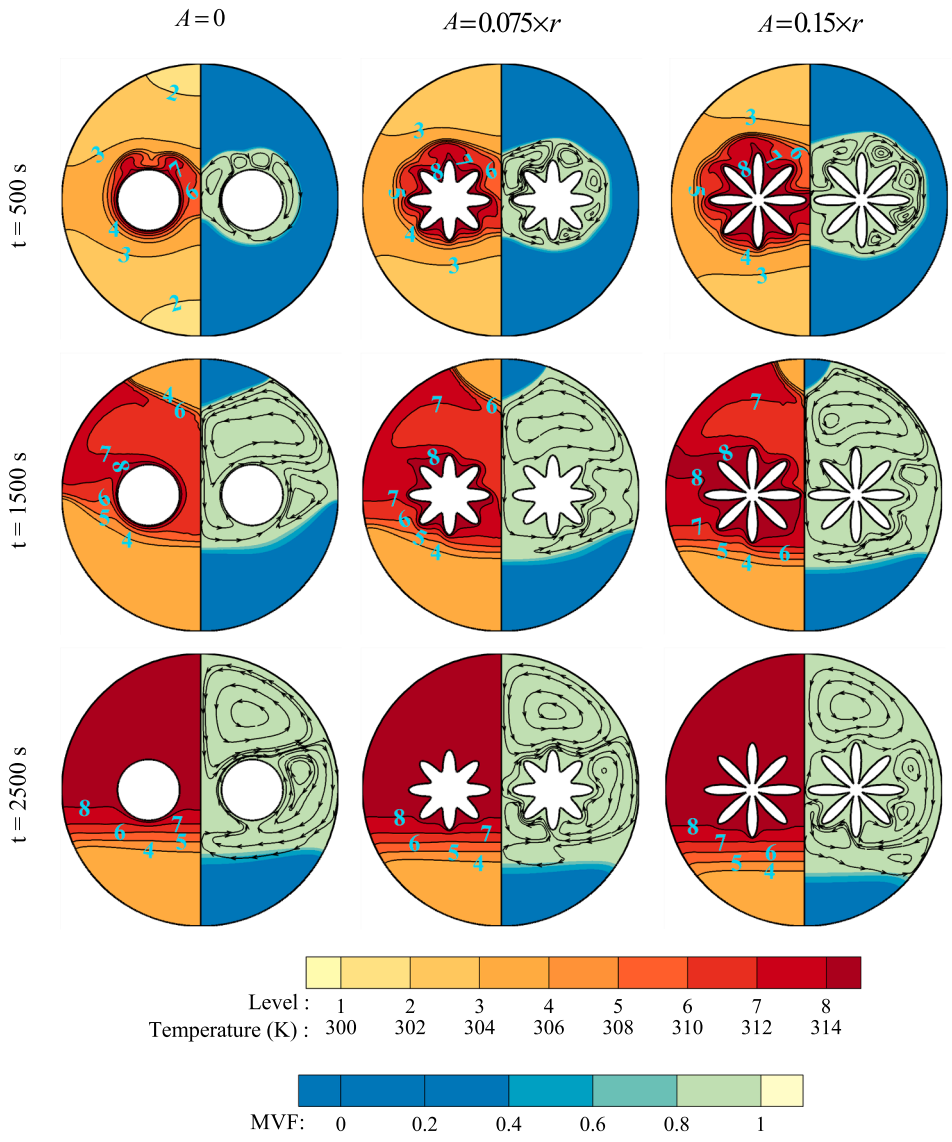

Fig. 17. The effect of amplitude on the isotherms, streamlines, and melt volume fraction for Cu nanoparticle when $\lambda = 8$, $\omega_{vf} = 0.08$ *and* $x_b = 0.375 \times r_s$.

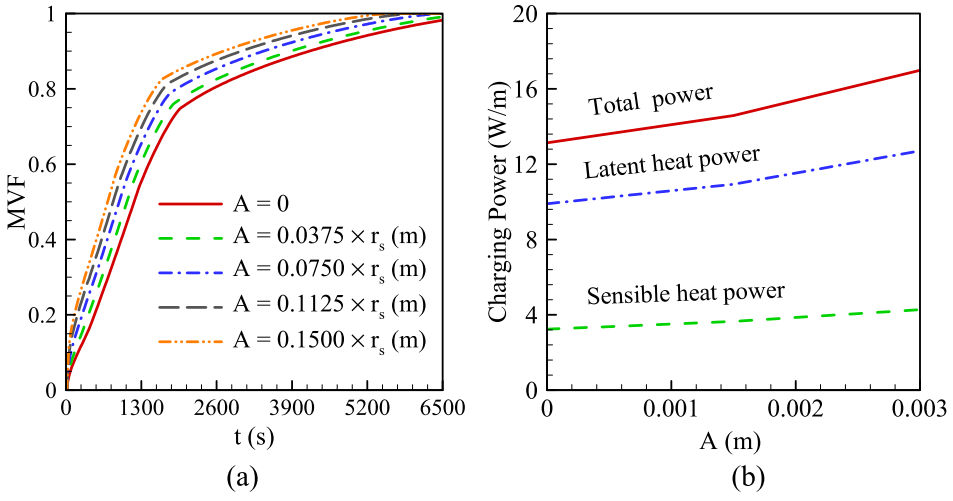

Fig. 18. The effect of amplitude on (a) *MVF* and (b) the charging power of Cu nanoparticle when $\omega_{vf} = 0.08, \lambda = 8$ *and* $x_b = 0.375 \times r_s$.

believe that the lack of a fully formed circulation zone has hindered the melting process when compared to the cases where the heated pipe is located either in the middle or close to the center. This observation is also reported in a numerical study by [15].

4.2.2. Distance between tubes

The effects of x_b on sensible, latent, and total power is displayed in Fig. 16b. It can be seen that, initially, the increase of x_b increases the amount of sensible, latent, and total power. A further increase of x_b over a certain value will result in a decrease of sensible, latent, and total power. The maximum charging power is obtained for an x_b value of 0.0091.

4.2.3. Amplitude of petals

Fig. 17 shows the impact of amplitude (A) on the isotherm's contours, liquid fraction, and streamline contours. A frequency of eight is selected for the cases using a quasi-petal heated pipe. When a circular heat pipe is used, four main recirculation zones are formed at $t = 500$s due to natural convection. When the circular heated pipe is replaced with a quasi-petal heated pipe, the heat transfer area increases; hence, the melting process is accelerated compared to the case with a circular pipe. It can also be observed that more recirculation zones are developed, which further strengthens the natural convection. As the amplitude increases, the heat transfer area increases even more, which leads to an accelerated melting process.

The evaluation of isotherms, melting liquid fractions, and streamlines at $t = 1500$s show the positive impact of enhancing the amplitude on the melting rate as a smaller solid PCM remains at the upper and lower sections of the container. As the melting continues, it can be seen that the solid PCM at the upper section is completely melted for all three cases. It should also be noted that a smaller solid PCM remains for the case with $A = 0.15r_s$, as expected.

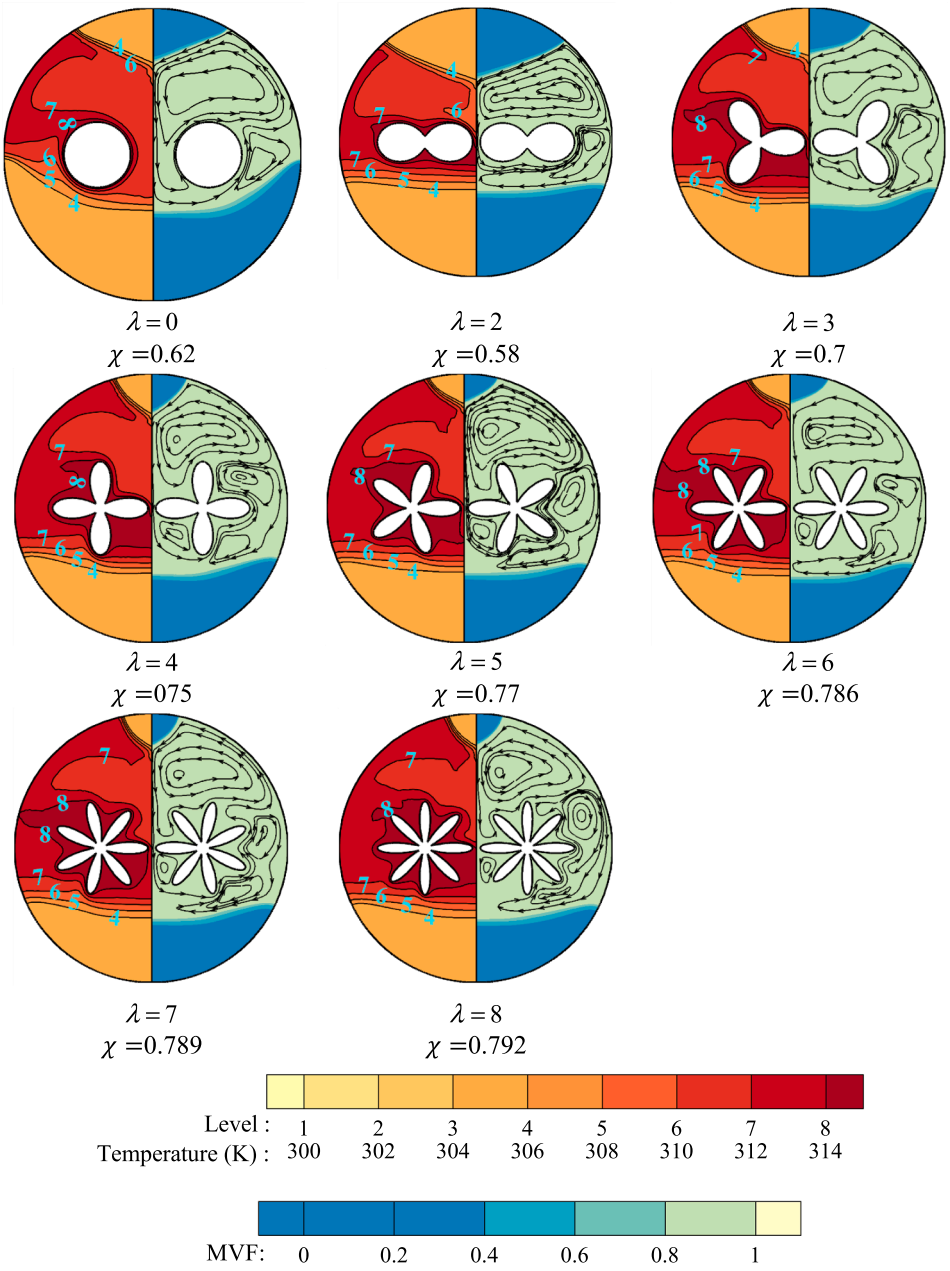

Fig. 19. The effect of frequency on the isotherms, streamline, and melt volume fraction for Cu nanoparticle at $t = 1500$s ($A = 0.15 \times r_s, \omega_{vf} = 0.08$ *and* $x_b = 0.375 \times r_s$).

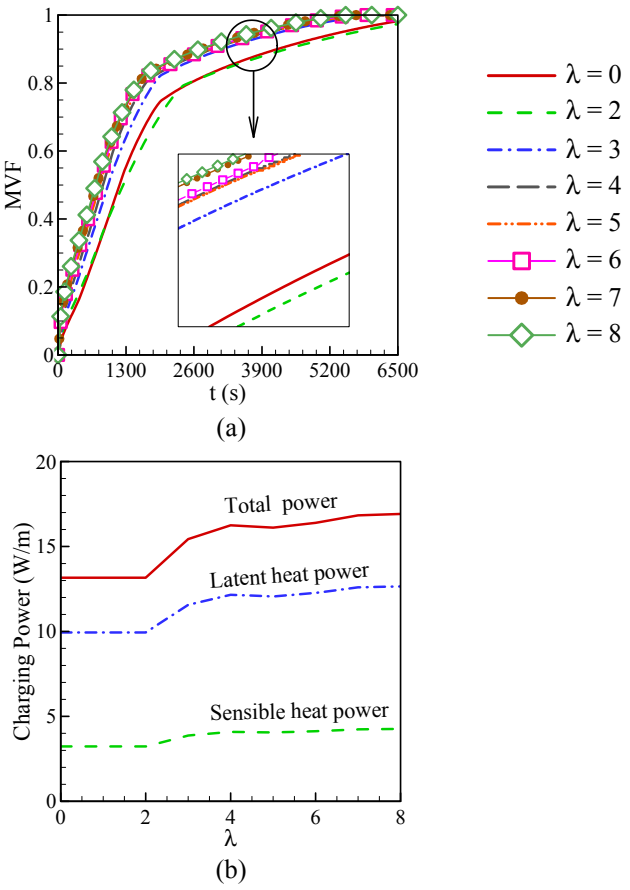

Fig. 20. The effect of amplitude on MVF and charging power for Cu nanoparticle ($A = 0.15 \times r_s$, $x_b = 0.375 \times r_s$ and $\omega_{vf} = 0.08$).

The liquid fraction history is plotted in Fig. 18a to provide a clearer understanding of the effect of amplitude on the melting process of the system. This figure also confirms that higher amplitude values result in faster melting rates. When an amplitude of $0.075r_s$ is used, it takes 6450 s for the entire PCM to melt. When the amplitude is doubled, this time decreases to 5550 s, which shows a 14% improvement. The sensible heat, latent heat, and the total charging power per unit width are plotted versus amplitude in Fig. 18b. The obtained results clearly show that the charging power, due to sensible heat and latent heat, increase with the increase in amplitude, which leads to larger total charging power. As the amplitude changes from 0 to 0.003 m, the charging power increases by 24% from 13 W/m to 17 W/m.

4.2.4. *Frequency of petals*

The influence of heated pipe petal frequency on streamlines, isotherms, and liquid fraction contours is presented at 1500 seconds after the start of the melting process in Fig. 19. To have a better understanding of the frequency effects, the liquid fraction and charging power variations versus time are also depicted in Fig. 20a and b. As the frequency increases from zero to two, the PCM liquid fraction either remains unchanged or decreases at some stages of the melting process.

The results obtained at $t = 1500s$ show that in the case with a circular-heated pipe, 62% of the PCM is melted, while for the case with a frequency of two, 58% of the PCM is melted. In general, more contact area is available with an increase in frequency, which facilitates the heat transfer from the heated pipe to the PCM. For the case with a frequency of two, the heat transfer surface is augmented; however, the heated pipe is wider, which may inhibit some of the formation of the natural convection recirculation zones between the heated pipe and the shell in the horizontal direction, as shown in Fig. 19. This issue does not exist as the frequency increases to three. At this frequency, the natural convection vortices are more developed when compared to the base case with a circular pipe, thereby increasing the speed of melting as confirmed by the obtained liquid fraction of 0.7. The variations between the results of the cases with frequencies of four, five, and six are negligible. This is likely due to the opposing effects of enhanced heat transfer surface and the suppression of natural convection. For frequencies over six, the effect of enhanced heat transfer surface and the resulting increase in natural convection becomes more pronounced, and the melting rates accelerate even more when compared to the other cases. An increase of 27% is observed in the melting rate when a circular heated pipe is replaced with a quasi-petal pipe with a frequency of eight.

Fig. 20b displays the effect of frequency on the charging power due to latent heat and sensible heat. This figure reveals that as the frequency increases over two, the sensible and latent power increases. This behavior can be explained by an increase in stored energy and a decrease in the melting time. Increasing the frequency from zero to eight will result in a 30 percent augmentation in charging power.

5. Conclusion

In the current investigation, a numerical simulation coupled with the Taguchi optimization method and analysis of variance was developed. The method was then implemented to analyze the effects of geometric parameters, as well as the dispersion of nano-additives, on the melting process in a heat exchanger energy storage unit. The main conclusions are listed below.

1. The optimum combination of the factors and levels leading to the highest value of the total energy storage is: $x_b/r_s = 0.375$, $A/r_s = 0.15$, $\lambda = 8$, $\omega_{vf} = 8\%$.
2. The geometric parameters contributed about 93.44% and 94.36% to the total energy storage for the copper and graphene oxide nano-additives, respectively.
3. Generally, the presence of nanoparticles could improve the melting rate smoothly. The impact of the nano-additives on energy storage power is lower than the geometric parameters. Based on an ANOVA analysis, the amplitude of petal shape could influence the total energy storage with a contribution ratio of about 41%, while the nanoparticles' contribution was 5–6%. Thus, using nanoparticles in the present design does not add much of an advantage. The copper nano-additives are more effective than the graphene oxide nano-additives.
4. The results of this study indicated that the geometric parameters should be considered as a primary factor when optimizing a heat exchanger energy storage system. An optimum design could lead to 22.5–23.3% energy storage improvement at a fixed charging time for 1400 s.
5. The results showed that locating the heated pipe close to the shell may hinder the natural convection effects, which leads to an increase in the melting time.
6. The melting rate decreases as the petal amplitude increases. An increase of 45% was obtained in the energy storage when a heated circular pipe and no nanoadditives was replaced with an optimum design (quasi-petal pipe and Cu NePCM).

Declaration of Competing Interest

The authors declare that they have no known competing financial interests or personal relationships that could have appeared to influence the work reported in this paper.

References

[1] Y. Li, N. Nord, Q. Xiao, T. Tereshchenko, Building heating applications with phase change material: a comprehensive review, J. Storage Mater. 31 (2020) 101634.
[2] F. Javadi, H. Metselaar, P. Ganesan, Performance improvement of solar thermal systems integrated with phase change materials (PCM), a review, Sol. Energy 206 (2020) 330–352.
[3] Y. Wu, X. Zhang, X. Xu, X. Lin, L. Liu, A review on the effect of external fields on solidification, melting and heat transfer enhancement of phase change materials, J. Storage Mater. 31 (2020) 101567.
[4] V.P. Katekar, S.S. Deshmukh, A review of the use of phase change materials on performance of solar stills, J. Storage Mater. 30 (2020) 101398.
[5] T. Xiong, L. Zheng, K.W. Shah, Nano-enhanced phase change materials (NePCMs): a review of numerical simulations, Appl. Therm. Eng. 115492 (2020).
[6] S.L. Tariq, H.M. Ali, M.A. Akram, M.M. Janjua, M. Ahmadlouydarab, Nanoparticles enhanced Phase Change Materials (NePCMs)-A Recent Review, Appl. Therm. Eng. 115305 (2020).
[7] S. Nižetić, M. Jurčević, M. Arıcı, A.V. Arasu, G. Xie, Nano-enhanced phase change materials and fluids in energy applications: a review, Renew. Sustain. Energy Rev. 129 (2020) 109931.
[8] B.E. Jebasingh, A.V. Arasu, A comprehensive review on latent heat and thermal conductivity of nanoparticle dispersed phase change material for low-temperature applications, Energy Storage Mater. 24 (2020) 52–74.
[9] L. Yang, J.-N. Huang, F. Zhou, Thermophysical properties and applications of nano-enhanced PCMs: an update review, Energy Convers. Manage. 214 (2020) 112876.
[10] M. Sheikholeslami, A. Zareei, M. Jafaryar, A. Shafee, Z. Li, A. Smida, I. Tlili, Heat transfer simulation during charging of nanoparticle enhanced PCM within a channel, Physica A 525 (2019) 557–565.
[11] A. Yehya, H. Naji, A novel technique to analyze the effect of enclosure shape on the performance of phase-change materials, Energy Procedia 75 (2015) 2131–2136.
[12] M. Bayat, M.R. Faridzadeh, D. Toghraie, Investigation of finned heat sink performance with nano enhanced phase change material (NePCM), Therm. Sci. Eng. Progr. 5 (2018) 50–59.
[13] N.S. Bondareva, B. Buonomo, O. Manca, M.A. Sheremet, Heat transfer performance of the finned nano-enhanced phase change material system under the inclination influence, Int. J. Heat Mass Transf. 135 (2019) 1063–1072.
[14] K. Hosseinzadeh, M. Alizadeh, D. Ganji, Solidification process of hybrid nano-enhanced phase change material in a LHTESS with tree-like branching fin in the presence of thermal radiation, J. Mol. Liq. 275 (2019) 909–925.
[15] Q. Ren, Enhancement of nanoparticle-phase change material melting performance using a sinusoidal heat pipe, Energy Convers. Manage. 180 (2019) 784–795.
[16] A. Awasthi, B. Kumar, H.H. Nguyen, S.S. Lee, J.D. Chung, Effect of sinusoidal cylindrical surface of PCM on melting performance, J. Mech. Sci. Technol. 34 (2020) 3395–3402.
[17] M. Sheikholeslami, M. Jafaryar, A. Shafee, H. Babazadeh, Acceleration of discharge process of clean energy storage unit with insertion of porous foam considering nanoparticle enhanced paraffin, J. Cleaner Prod. 261 (2020) 121206.
[18] R.B. Mahani, H.I. Mohammed, J.M. Mahdi, F. Alamshahi, M. Ghalambaz, P. Talebizadehsardari, W. Yaïci, Phase change process in a zigzag plate latent heat storage system during melting and solidification, Molecules 25 (2020) 4643.
[19] R.P. Singh, H. Xu, S. Kaushik, D. Rakshit, A. Romagnoli, Charging performance evaluation of finned conical thermal storage system encapsulated with nano-enhanced phase change material, Appl. Therm. Eng. 151 (2019) 176–190.
[20] J. Alinejad, J.A. Esfahani, Taguchi design of three dimensional simulations for optimization of turbulent mixed convection in a cavity, Meccanica 52 (2017) 925–938.
[21] M. Sobhani, H.A. Tighchi, J.A. Esfahani, Taguchi optimization of combined radiation/natural convection of participating medium in a cavity with a horizontal fin using LBM, Physica A 509 (2018) 1062–1079.
[22] I. Zahmatkesh, M.R.H. Shandiz, Optimum constituents for MHD heat transfer of nanofluids within porous cavities, J. Therm. Anal. Calorim. 138 (2019) 1669–1681.
[23] R. Nath, M. Krishnan, Optimization of double diffusive mixed convection in a BFS channel filled with Alumina nanoparticle using Taguchi method and utility concept, Sci. Rep. 9 (2019) 1–19.
[24] L. Tang, J. Pan, B. Sundén, Parametric study and optimization on heat transfer and flow characteristics in a rectangular channel with longitudinal vortex generators, Numer. Heat Transfer, Part A: Appl. 76 (2019) 830–850.
[25] A.H. Sharifi, I. Zahmatkesh, A.M. Mozhdehi, A. Morsali, F.F. Bamoharram, Stability appraisement of the alumina-brine nanofluid in the presence of ionic and non-ionic disparents on the alumina nanoparticles surface as heat transfer fluids: quantum mechanical study and Taguchi-optimized experimental analysis, J. Mol. Liq. 113898 (2020).
[26] N. Biçer, T. Engin, H. Yaşar, E. Büyükkaya, A. Aydın, Design optimization of a shell-and-tube heat exchanger with novel three-zonal baffle by using CFD and taguchi method, Int. J. Therm. Sci. 155 (2020) 106417.
[27] M. Hosseinzadeh, A. Faezian, S.M. Mirzababaee, H. Zamani, Parametric analysis and optimization of a portable evacuated tube solar cooker, Energy 194 (2020) 116816.
[28] A. Hussanan, M.Z. Salleh, I. Khan, S. Shafie, Convection heat transfer in micropolar nanofluids with oxide nanoparticles in water, kerosene and engine oil, J. Mol. Liq. 229 (2017) 482–488.
[29] K. Kant, A. Shukla, A. Sharma, P.H. Biwole, Heat transfer study of phase change materials with graphene nano particle for thermal energy storage, Sol. Energy 146 (2017) 453–463.
[30] H.C. Brinkman, The viscosity of concentrated suspensions and solutions, J. Chem. Phys., 20 (1952) 571-571.
[31] H.Ş. Aybar, M. Sharifpur, M.R. Azizian, M. Mehrabi, J.P. Meyer, A review of thermal conductivity models for nanofluids, Heat Transfer Eng. 36 (2015) 1085–1110.
[32] J.N. Reddy, D.K. Gartling, The finite element method in heat transfer and fluid dynamics, CRC Press, 2010.
[33] O.C. Zienkiewicz, R.L. Taylor, P. Nithiarasu, The finite element method for fluid dynamics, Elsevier, 2015.
[34] J.C. De Los Reyes, S. González Andrade, A combined BDF-semismooth Newton approach for time-dependent Bingham flow, Numer. Methods Partial Differential Equations 28 (2012) 834–860.
[35] O. Schenk, K. Gärtner, Solving unsymmetric sparse systems of linear equations with PARDISO, Future Generation Comput. Syst. 20 (2004) 475–487.
[36] P. Wriggers, Nonlinear finite element methods, Springer Science & Business Media, 2008.
[37] F. Verbosio, A. De Coninck, D. Kourounis, O. Schenk, Enhancing the scalability of selected inversion factorization algorithms in genomic prediction, J. Computational Sci. 22 (2017) 99–108.
[38] L. Kumar, B.S. Manjunath, R.J. Patel, S.G. Markandeya, R.G. Agrawal, A. Agrawal, Y. Kashyap, P.S. Sarkar, A. Sinha, K.N. Iyer, S.V. Prabhu, Experimental investigations on melting of lead in a cuboid with constant heat flux boundary condition using thermal neutron radiography, Int. J. Therm. Sci. 61 (2012) 15–27.
[39] O. Bertrand, B. Binet, H. Combeau, S. Couturier, Y. Delannoy, D. Gobin, M. Lacroix, P. Le Quéré, M. Médale, J. Mencinger, H. Sadat, G. Vieira, Melting driven by natural convection A comparison exercise: first results, Int. J. Therm. Sci. 38 (1999) 5–26.
[40] T.H. Kuehn, R.J. Goldstein, An experimental and theoretical study of natural convection in the annulus between horizontal concentric cylinders, J. Fluid Mech. 74 (1976) 695.
[41] S. Kashani, A. Ranjbar, M. Abdollahzadeh, S. Sebti, Solidification of nano-enhanced phase change material (NEPCM) in a wavy cavity, Heat Mass Transf. 48 (2012) 1155–1166.
[42] M. Ezoddin, J.Å. Jönsson, A. Kyani, Equilibrium sampling through membrane based on a hollow fiber for determination of naproxen and diclofenac in sludge slurry using Taguchi orthogonal array experimental design, Desalin. Water Treat. 52 (2014) 2472–2480.
[43] R.K. Roy, Design of Experiments Using The Taguchi Approach: 16 Steps to Product and Process Improvement, Wiley, 2001.
[44] K. Hinkelmann, Design and analysis of experiments, volume 3: special designs and applications, John Wiley & Sons, 2012.
[45] S.B. Otieno, C.M. Anderson-Cook, Design and analysis of experiments for directional data, Design and Analysis of Experiments: Special Designs and Applications, John Wiley & Sons Inc., Hoboken, New Jersey, 2012, pp. 501–532.
[46] V. Mayilvelnathan, A.V. Arasu, Experimental investigation on thermal behavior of graphene dispersed erythritol PCM in a shell and helical tube latent energy storage system, Int. J. Therm. Sci. 155 (2020) 106446.
[47] B. Akhmetov, M. Navarro, A. Seitov, A. Kaltayev, Z. Bakenov, Y. Ding, Numerical study of integrated latent heat thermal energy storage devices using nanoparticle-enhanced phase change materials, Sol. Energy 194 (2019) 724–741.